Supplementary Materials for **Freely manipulating on-chip sources by intelligent-algorithm vectorial metasurfaces based on an identity scheme**

1 Intelligent Algorithm

The proposed metasurface is a vectorial metasurface that can simultaneously control the intensity and polarization distributions of the far field utilizing identical nanogrooves as nano-scatterers. We propose the Intelligent Algorithm to arrange the identical nano-scatterers and optimize the performance. The algorithm contains two major steps : the Iterative Algorithm (see subsection 1.1) adapted from the mixed-region amplitude freedom (MRAF) algorithm[1] to generate amplitude distributions with quasi-discrete features on the metasurface, and the Post-Processing Algorithm (see subsection 1.2) to arrange a set of nano-scatterers on the metasurface to approximate this amplitude distribution.

1.1 Iterative Algorithm

1.1.1 Main Process of the Iterative Algorithm

We use $\boldsymbol{J}(x, y)$ to represent the vector field distribution in the metasurface plane (i.e., the plane where the metasurface structure is located), and $\boldsymbol{A}(k_x, k_y)$ to represent the vector field distribution in the far field (i.e., on the Fourier plane). Here we divide the metasurface plane into a grid of size $N \times N$ for numerical iteration purposes. Then, we decompose the vector field into LCP (left circular polarization) and RCP (right circular polarization) components. For example, $\boldsymbol{A}(k_x, k_y) = A_L \left|L\right\rangle + A_R \left|R\right\rangle$, where $\left|L\right\rangle$ and $\left|R\right\rangle$ represent the unit polarization vectors for the LCP and RCP components, respectively. The IFTA (Iterative Fourier Transform Algorithm) adopted in this algorithm controls the polarization distribution by adjusting the phase difference and relative amplitude between the LCP and RCP components, while their overall phase is a free variable that does not affect the polarization distribution. The target far-field distribution is denoted as $\boldsymbol{A}^{(id)}(k_x, k_y)$, which is specified by the designer. Below, we outline the main steps of the iterative algorithm.

To begin with, the metasurface plane is randomly assigned a vector field $[\mathrm{rand}(N, N)\left|L\right\rangle + \mathrm{rand}(N, N)\left|R\right\rangle]$ as an initial state. Here, $\mathrm{rand}(N, N)$ represents a random real number matrix with size of $N \times N$. Subsequently, a definite phase distribution $\phi_0(x, y)$ is assigned to the light field in the metasurface plane. This phase distribution is determined by the physical settings of the metasurface. In this study, the metasurface is excited by a z-polarized electric dipole located

at the center. The radiation field of the dipole first couples into the SPP wave on the metal surface and isotropically propagates radially outward. The outer nano-scatterers then scatter the SPP wave into the far field. Therefore, the phase distribution satisfies $\phi_0(x,y) = kr(x,y) = k\sqrt{x^2+y^2}$, where k is the SPP wave vector. In principle, the algorithm presented here can be applied to other forms of metasurfaces by setting $\phi_0(x,y)$ to be the actual phase in the metasurface plane. With the phase distribution determined, the initial vector field in the metasurface plane can be expressed as $\boldsymbol{J}^{(0)}(x,y) = e^{i\phi_0(x,y)}\left(\mathrm{rand}(N,N)\,|L\rangle + \mathrm{rand}(N,N)\,|R\rangle\right)$.

In each iteration, a Fourier transform is applied to $\boldsymbol{J}^{(n)}(x,y)$ to obtain the far field as $\boldsymbol{A}^{(n)}(k_x,k_y) = \mathcal{F}\{\boldsymbol{J}^{(n)}(x,y)\}$, where $\mathcal{F}$ denotes the Fourier transform. The *similarity* between $\boldsymbol{A}^{(n)}(k_x,k_y)$ and the target far-field distribution $\boldsymbol{A}^{(id)}(k_x,k_y)$ is evaluated (see subsubsection 1.1.2) as $\mathrm{sim}(\boldsymbol{A}^{(n)},\boldsymbol{A}^{(id)})$. If the similarity reaches convergence, the iteration is stopped and the post-processing algorithm begins (see subsection 1.2); otherwise, the iteration continues.

To ensure that the far-field distribution converges towards the target distribution $\boldsymbol{A}^{(id)}(k_x,k_y)$, the `MRAF` algorithm[1] is employed. In each iteration, a proportion of the desired target far-field distribution $\boldsymbol{A}^{(id)}(k_x,k_y)$ is introduced into the current far-field distribution, until the final distribution converges to the target. The specific mixing form is given by:

$$\boldsymbol{A}'^{(n)} = \left\{ m\boldsymbol{A}^{(id)}\Big|_{\mathrm{SR}} \cdot e^{i\phi^{(n)}(k_x,k_y)} + (1-m)\boldsymbol{A}^{(n)}|_{\mathrm{NR}} \right\}. \tag{S1}$$

Here, the subscript SR stands for Signal Region, and NR represents Noise Region[1]. The parameter $m \in [0,1]$ is the mixing parameter, indicating the amplitude proportion of the mixed-in target field component. The value of m is scanned to achieve optimal results. According to Equation S1, the optical phase distribution of the far field is adjusted in each iteration to optimize the far field in the Signal Region with the designed intensity and polarization distributions. To ensure convergence of the iterative process, we adopt a special phase assignment method for the mixed-in target field $\boldsymbol{A}^{(id)}$. This involves projecting the current far field onto the target distribution and extracting the phase denoted as $\phi^{(n)}(k_x,k_y)$. For detailed information on this phase assignment method, see subsubsection 1.1.3.

In the next step, the new vector field $\boldsymbol{A}'^{(n)}(k_x,k_y)$ is subjected to an inverse Fourier transform to obtain the vector field in the metasurface plane $\boldsymbol{J}'^{(n)}(x,y) = \mathcal{F}^{-1}\left[\boldsymbol{A}'^{(n)}(k_x,k_y)\right]$. The total light intensity in the metasurface plane is then calculated by $I'^{(n)} = \int \left|\boldsymbol{J}'^{(n)}(x,y)\right|^2 \mathrm{d}x\mathrm{d}y$.

Unlike traditional iterative algorithms where the field in the metasurface plane $\boldsymbol{J}'^{(n)}(x,y)$ is directly substituted into the next iteration, an additional step for polarization projection of the light field distribution in the metasurface plane is specially incorporated in the algorithm here. The reason is that $\boldsymbol{J}'^{(n)}(x,y)$ usually possesses an intricate polarization distribution during iteration, as shown in inset I of Figure 2 in the main manuscript. However, the actual structure of the proposed metasurface comprises nanogrooves with their long edges forming angles of $-45°$ and $+45°$ with the radial direction (as shown in Figure 1b in the main manuscript), emitting linearly polarized light. To ensure convergence to this locally linear polarization, a polarization mask, as illustrated in inset II of Figure 2 in the main manuscript, is specially introduced into the algorithm. This polarization mask consists of azimuthally alternating blue (P_1) and red (P_2) sub-areas. In these sub-areas, only linearly polarized components angled $+45°$ or $-45°$ with respect to radial direction are retained. We denote these two polarization states as $|P_1\rangle$ and $|P_2\rangle$, and they are

a set of orthogonal basis in the local coordinate when neglecting the radial direction difference between adjacent sub-areas. Thus, $\boldsymbol{J}'^{(n)}(x,y)$ can be decomposed as $\boldsymbol{J}'^{(n)}(x,y) = J'^{(n)}_{P_1}|P_1\rangle + J'^{(n)}_{P_2}|P_2\rangle$. Subsequently, masking functions are applied in different masked regions to extract the corresponding amplitudes, effectively projecting $\boldsymbol{J}'^{(n)}(x,y)$ to sub-area-wise local polarization state:

$$J''^{(n)}_{P_1}(x,y) = |J'^{(n)}_{P_1}(x,y)| \cdot \mathrm{mask}_{P_1}(x,y), \tag{S2}$$

$$J''^{(n)}_{P_2}(x,y) = |J'^{(n)}_{P_2}(x,y)| \cdot \mathrm{mask}_{P_2}(x,y). \tag{S3}$$

Here, $\mathrm{mask}_{P_1}(x,y)$ and $\mathrm{mask}_{P_2}(x,y)$ are the masking functions used for sub-area P_1 and P_2, respectively. These functions take the value of 1 inside sub-areas, while elsewhere they remain 0. In this work, sub-area P_1 and P_2 resemble sectoral strip shapes with alternating azimuthal distribution due to the point source geometry. Equation S2 and Equation S3 extract the modulus of $J'^{(n)}_{P_1}$ and $J'^{(n)}_{P_2}$ as the new complex amplitudes of the linearly polarized light fields within the corresponding sub-areas. The masking function nullifies the orthogonal polarization components within the sub-area and the amplitudes outside the sub-area. After applying the polarization mask, the new vector field in the metasurface plane is $\boldsymbol{J}''^{(n)} = J''^{(n)}_{P_1}|P_1\rangle + J''^{(n)}_{P_2}|P_2\rangle$. We re-calculate the total light intensity in the metasurface plane $I''^{(n)}$. Its value decreases compared to the value of $I'^{(n)}$, because of the application of the polarization mask. Therefore, we rescale the amplitudes in the metasurface plane accordingly to ensure the total light intensity before and after mask application remains constant:

$$\boldsymbol{J}'''^{(n)} = \sqrt{\frac{I'^{(n)}}{I''^{(n)}}} \cdot \boldsymbol{J}''^{(n)}. \tag{S4}$$

This amplitude rescaling operation turns out to be crucial in improving the convergence of the iterative process. We now have $\boldsymbol{J}'''^{(n)}$ in the metasurface plane, and a similar procedure that set phase in the metasurface plane to be $\phi_0(x,y)$ is executed. Finally, we make this to be the input of the next iteration:

$$\boldsymbol{J}^{(n+1)} = \boldsymbol{J}'''^{(n)}\Big|_{\phi\to\phi_0(x,y)}. \tag{S5}$$

Upon convergence of the iteration, the iteration program exits the loop and provides the converged optical field in the metasurface plane $\boldsymbol{J}(x,y)$ as the output. This solution contains both the amplitude and polarization state information in the metasurface plane. Its polarizations in sub-areas P_1 and P_2 are the preset $+45°$ and $-45°$ linear polarization states, respectively. The amplitude is non-zero only within sub-areas P_1 and P_2. These quasi-discrete distributions of polarization and amplitude lay the groundwork for further post-processing algorithm where $\boldsymbol{J}(x,y)$ are approximately replaced by discrete nanogrooves oriented at $-45°$ and $+45°$ to the radial direction.

1.1.2 Evaluation Function and Convergence Criterion of the Iterative Algorithm

The evaluation function is a scalar function used to measure the consistency between a given far field $\boldsymbol{A}(k_x,k_y)$ and the target far field $\boldsymbol{A}^{(id)}(k_x,k_y)$. In the proposed algorithm, *similarity* is

employed as the evaluation function and serves as the criterion for determining the convergence of the iteration.

Firstly, we define the *scalar similarity* between two scalar optical field distributions. For two scalar complex matrices of equal size $A, B \in \mathbb{C}^{N\times N}$, the scalar similarity is defined as:

$$\mathrm{sim}(A,B) \equiv \mathrm{corrcoef}(|A|,|B|)_{1,2} \in [0,1], \tag{S6}$$

where corrcoef is the correlation coefficient function, $||$ stands for element-wise norm, and the subscript $1,2$ represents the element in the first row and second column of the correlation coefficient matrix. A larger similarity indicates that the scalar fields described by the two matrices are closer to each other.

We further define the similarity between two vector field distributions. For two complex vector fields with identical dimensions $\boldsymbol{A}, \boldsymbol{B} \in \mathbb{C}^{N\times N\times 2}$, the vectorial similarity is defined as:

$$\begin{aligned} &\mathrm{sim}(\boldsymbol{A},\boldsymbol{B}) \equiv \frac{1}{2}\left(\mathrm{sim}\left(A_L,B_L\right)+\mathrm{sim}\left(A_R,B_R\right)\right), \\ &\boldsymbol{A} = A_L\left|L\right\rangle + A_R\left|R\right\rangle, \quad \boldsymbol{B} = B_L\left|L\right\rangle + B_R\left|R\right\rangle. \end{aligned} \tag{S7}$$

Here we decompose the vector field into a superposition of LCP and RCP components and define the average of the scalar similarities of the LCP and RCP components as the vectorial similarity. We do not consider the phase difference between the LCP and RCP components here because the phase difference between the LCP and RCP components of the mixed-in target light field is set to the designed values during the mixing process in iteration loops; therefore, the vectorial similarity only needs to assess the amplitude distributions of each polarization component.

1.1.3 Phase Assignment Method for Far-Field Mixing in Iterative Algorithms

According to Equation S1, the intensity and polarization distributions of the target far field $\boldsymbol{A}^{(id)}$ are directly introduced into the Signal Region in each iteration. The additional phase distribution $\phi^{(n)}$ of the far field in the Signal Region is assigned using the following expression:

$$\phi^{(n)}(k_x,k_y) = \arg\left(A_L^{(id)^*}\cdot A_L^{(n)} + A_R^{(id)^*}\cdot A_R^{(n)}\right), \tag{S8}$$

where $\boldsymbol{A}^{(n)}(k_x,k_y) = A_L^{(n)}\left|L\right\rangle + A_R^{(n)}\left|R\right\rangle$ and $\boldsymbol{A}^{(id)}(k_x,k_y) = A_L^{(id)}\left|L\right\rangle + A_R^{(id)}\left|R\right\rangle$ are the decomposition of the current far field $\boldsymbol{A}^{(n)}$ and the target far field $\boldsymbol{A}^{(id)}$, respectively. We further define the corresponding normalized polarization state $\boldsymbol{\lambda}^{(n)} = \left|\lambda^{(n)}\right\rangle = \frac{1}{\sqrt{|A_L^{(n)}|^2+|A_R^{(n)}|^2}}\left(A_L^{(n)}\left|L\right\rangle + A_R^{(n)}\left|R\right\rangle\right)$ and $\boldsymbol{\lambda}^{(id)} = \left|\lambda^{(id)}\right\rangle = \frac{1}{\sqrt{|A_L^{(id)}|^2+|A_R^{(id)}|^2}}\left(A_L^{(id)}\left|L\right\rangle + A_R^{(id)}\left|R\right\rangle\right)$. These two normalized polarization states describe the complex polarization distributions of the current far field and the target far field. Thus, we can rewrite Equation S1 as:

$$\boldsymbol{A}'^{(n)} = \left\{ m\,\frac{|\boldsymbol{A}^{(id)}|}{|\left\langle\lambda^{(id)}\middle|\lambda^{(n)}\right\rangle|}\cdot\hat{P}^{(id)}\boldsymbol{\lambda}^{(n)}\Big|_{\mathrm{SR}} + (1-m)\boldsymbol{A}^{(n)}\Big|_{\mathrm{NR}} \right\}. \tag{S9}$$

Here, $|\boldsymbol{A}^{(id)}| = \sqrt{|A_L^{(id)}|^2+|A_R^{(id)}|^2}$ is the amplitude distribution of the target far field; the projection operator $\hat{P}^{(id)} = \left|\lambda^{(id)}\right\rangle\left\langle\lambda^{(id)}\right|$ projects any polarization state onto target polarization

state. Thus, the proposed phase assignment method implies that, the current far field $\boldsymbol{A}^{(n)}$ is projected onto the polarization state of the target far field $\boldsymbol{A}^{(id)}$ at each far-field position (in the signal region) during mixing. Then, the phase of the projected component is exacted and assigned to the mixed-in field. This complex far-field-position-dependent phase assignment method ensures that, the proportion of the target polarization state progressively increases at each far-field position (in the signal region). Therefore, the polarization purity of the target polarization state approaches 1 at each far-field position (in the signal region) as the iteration converges. In contrast, traditional algorithms typically assign the phase of a fixed component without distinction over different far-field positions, such as the phase assignment of the LCP component to the newly introduced target far-field in the MRAF mixing process. However, if the target polarization is RCP at a specific far-field position, the LCP component will approach zero near convergence, leading to poorer LCP phase stability and poorer algorithm convergence. Therefore the proposed phase assignment strategy dependent on far-field position is more suitable for designing target light fields with complex polarization distributions, which ensures the MRAF mixing algorithm converges robustly with exact polarization distributions.

1.1.4 Summary of the Iterative Algorithm

Algorithm 1 IFTA with Polarization Masks

Inputs:

$\boldsymbol{A}^{(id)}$: designed target far field; $\phi_0(x,y)$: phase distribution in the metasurface plane.

Initialize:

$\boldsymbol{J}^{(0)}(x,y) = e^{i\phi_0(x,y)} \left(\mathrm{rand}(N,N)\,|L\rangle + \mathrm{rand}(N,N)\,|R\rangle\right)$.

repeat

Obtain last iteration result $\boldsymbol{J}^{(n-1)}(x,y)$; set phase $\boldsymbol{J}^{(n)}(x,y) = e^{i\phi_0}|\boldsymbol{J}^{(n-1)}|$;

Fourier transform $\boldsymbol{A}^{(n)}(k_x,k_y) = \mathcal{F}\{\boldsymbol{J}^{(n)}(x,y)\}$;

Extract local phase $\phi^{(n)}(k_x,k_y) = \arg\left(A_L^{(id)^*}\cdot A_L^{(n)} + A_R^{(id)^*}\cdot A_R^{(n)}\right)$;

MRAF mixing $\boldsymbol{A'}^{(n)} = \left\{ m\boldsymbol{A}^{(id)}\big|_{\mathrm{SR}}\cdot e^{i\phi^{(n)}(k_x,k_y)} + (1-m)\boldsymbol{A}^{(n)}|_{\mathrm{NR}}\right\}$;

Inverse fourier transform $\boldsymbol{J'}^{(n)}(x,y) = \mathcal{F}^{-1}\left[\boldsymbol{A'}^{(n)}(k_x,k_y)\right]$;

Compute total intensity $I'^{(n)} = \int \left|\boldsymbol{J'}^{(n)}(x,y)\right|^2 \mathrm{d}x\mathrm{d}y$;

Project onto local orthogonal basis $\boldsymbol{J'}^{(n)}(x,y) = J'^{(n)}_{P_1}\,|P_1\rangle + J'^{(n)}_{P_2}\,|P_2\rangle$;

Apply polarization mask $J''^{(n)}_{P_\alpha}(x,y) = |J'^{(n)}_{P_\alpha}(x,y)|\cdot \mathrm{mask}_{P_\alpha}(x,y), \quad \alpha = 1,2$;

Compose local orthogonal basis $\boldsymbol{J''}^{(n)} = J''^{(n)}_{P_1}\,|P_1\rangle + J''^{(n)}_{P_2}\,|P_2\rangle$;

Compute total intensity $I''^{(n)} = \int \left|\boldsymbol{J''}^{(n)}(x,y)\right|^2 \mathrm{d}x\mathrm{d}y$;

Rescale amplitude to maintain intensity $\boldsymbol{J'''}^{(n)} = \sqrt{\frac{I'^{(n)}}{I''^{(n)}}}\cdot \boldsymbol{J''}^{(n)}$;

$\boldsymbol{J}^{(n)}(x,y) = \boldsymbol{J'''}^{(n)}$ is the new iteration result.

until Similarity $\mathrm{sim}(\boldsymbol{A}^{(n)}, \boldsymbol{A}^{(id)})$ converges.

Output:

$\boldsymbol{J}(x,y)$: Intensity & polarization distribution in the metasurface plane.

1.2 Discretized Post-Processing Algorithm

1.2.1 Main Process

After obtaining the field distribution in the metasurface plane through the iterative algorithm described in subsection 1.1, we perform the post-processing algorithm as the second step. This step involves mapping the field distribution onto a real physical system involving discrete nano-scatterers. The high-spatial-resolution field is then approximated by the scattered field from a finite number of nano-scatterers such as nanogrooves.

The iterative algorithm gives the converged vector field in the metasurface plane, denoted as $\boldsymbol{J}(x,y)$, which serves as the input for the post-processing algorithm. Within sub-areas P_1 and P_2, $\boldsymbol{J}(x,y)$ are $+45°$ and $-45°$ (with respect to radial direction) linearly polarized lights with complex amplitudes represented by J_{P_1} and J_{P_2}, respectively. To facilitate the conversion from a complex amplitude distribution to several discrete, identical nano-scatterers, a certain effective amplitude threshold t_1 is first set. Each of the polarization components, J_{P_1} and J_{P_2}, individually undergo a threshold cutoff where the field amplitude less than the threshold is set to zero:

$$J^{cut}_{\substack{P_\alpha \\ \alpha=1,2}}(x,y) = \begin{cases} 0 & \text{, if } |J_{P_\alpha}(x,y)| < t_1 \cdot \max_{(x,y)} |J_{P_\alpha}(x,y)|; \\ J_{P_\alpha}(x,y) & \text{, otherwise.} \end{cases} \tag{S10}$$

Here, $t_1 \in (0,1)$ is the threshold parameter. Since the previous iterative algorithm uses polarization masks to partition the field in the metasurface plane along the azimuthal direction, and the phase distribution $\phi_0(x,y) = kr(x,y)$ induces quasi-periodic characteristic in the amplitude along the radial direction, the field $\boldsymbol{J}(x,y)$ exhibits quasi-discrete feature in its amplitude distribution. After applying threshold cutoff operation, discrete "island-like" regions with subwavelength sizes emerge, as illustrated in inset V of Figure 2 in the main manuscript.

Subsequently, for each "island-like" region, we use individual nano-scatterer to approximate the sum of the complex amplitudes within each region, as illustrated in inset VI of Figure 2 in the main manuscript. First, a breadth-first search algorithm (BFS) is employed to analyze the connectivity of the cutted-off amplitude $\boldsymbol{J}^{cut}_{P_\alpha}(x,y), \alpha \in \{1,2\}$. This results in a series of *connected blocks* $\mathrm{blk}_i(\bar{x}_i, \bar{y}_i)$ containing a set of connected pixels labeled by the index i, where $(\bar{x}_i, \bar{y}_i)$ representing the amplitude-modulus-weighted average of all pixel coordinates within blk_i. The sum of the complex amplitudes of all pixels in blk_i is designated as the complex amplitude $\widetilde{E}_i$. The above definitions are formulated as:

$$\begin{aligned} (\bar{x}_i, \bar{y}_i) &= \frac{\sum_{(x,y)\in \mathrm{blk}_i} \left| J^{cut}_{P_\alpha}(x,y) \right| \cdot (x,y)}{\sum_{(x,y)\in \mathrm{blk}_i} \left| J^{cut}_{P_\alpha}(x,y) \right|}, \\ \widetilde{E}_i &= \sum_{(x,y)\in \mathrm{blk}_i} J^{cut}_{P_\alpha}(x,y). \end{aligned} \tag{S11}$$

Then, a threshold cutoff operation is again applied to each connected block blk_i with a threshold parameter $t_2 \in (0,1)$:

$$\mathrm{blk}_i = \begin{cases} \text{delete} & \text{, if } |\widetilde{E}_i| < t_2 \cdot \max_j |\widetilde{E}_j|; \\ \text{keep} & \text{, otherwise.} \end{cases} \tag{S12}$$

In this step, connected blocks blk_i with total complex amplitudes $|\widetilde{E}_i|$ below a certain threshold are deleted. These connected blocks correspond to regions that either have a very small physical area or a relatively weak sum of complex amplitudes. Through this operation, the procedure retains only those connected blocks that significantly contribute to the emission, thereby reducing the number of discrete nano-scatterers and minimizing unnecessary scattering losses caused by inefficient nano-scatterers arrangement.

The block coordinate $(\bar{x}_i, \bar{y}_i)$ obtained from Equation S11 is approximately located at the center of each connected block. However, it does not accurately reproduce the phase of the scattered field $\widetilde{E}_i$ of each connected blocks by directly placing nano-scatterers at these positions. To have good reconstruction quality, we want to make the phase of the scattered field remains unchanged before and after substitution. For the axisymmetric system considered in this paper, the phase of the scattered light from a nano-scatterer in the metasurface plane $\phi_0(x, y) = kr(x, y)$ depends solely on its radial position r. Hence, we keep the azimuthal position of the nano-scatterers unchanged and make a slight radial adjustment to the coordinates from $(\bar{x}_i, \bar{y}_i)$ to $(\bar{x}_i^f, \bar{y}_i^f)$ to be defined as:

$$(\bar{x}_i^f, \bar{y}_i^f) = \left(1 + \frac{\delta r}{\sqrt{\bar{x}_i^2 + \bar{y}_i^2}}\right) \cdot (\bar{x}_i, \bar{y}_i), \tag{S13}$$

where $\delta r \in [-\lambda/2, \lambda/2]$ represents the radial shift. This adjustment ensures that, by moving the nano-scatterer within a wavelength's range radially, we can always satisfy:

$$\phi_0(\bar{x}_i^f, \bar{y}_i^f) = \arg(\widetilde{E}_i), \tag{S14}$$

which means that placing a nano-scatterer at the fine-tuned position $(\bar{x}_i^f, \bar{y}_i^f)$ ensures that the phase of its scattered field equals the phase of the total scattered field of a connected block, $\arg(\widetilde{E}_i)$. This nano-scatterer's scattered field can then approximate the field within a subwavelength-scale connected block blk_i. As the far-field reconstruction is highly sensitive to the phase of each nano-scatterer, the aforementioned position fine-tuning process significantly enhances the reconstruction quality of the far field. Additionally, since the shift distance during fine-tuning does not exceed half of the SPP wavelength, it does not substantially alter the distribution of the scattered field.

1.2.2 Scanning of Threshold Parameters t_1, t_2

In the post-processing algorithm in subsection 1.2, there are two adjustable parameters, namely the cutoff thresholds t_1 and t_2. To achieve optimal performance, the algorithm conducts a scan of these parameters and selects the best result based on an evaluation function (here we chose it to be the similarity function detailed in subsubsection 1.1.2). Figure S1 displays the parameter scanning results for the metasurface with four-channel emission in the far field. When $t_1 = 0.06$ and $t_2 = 0.21$, the best performance is obtained. In the parameter scanning process, the SPP attenuation effect (as SPP propagates outward radially, its amplitude continuously attenuates due to inherent cylindrical decay law alongside Ohmic and scattering losses) has been taken into account. This operation is implemented by employing a simple empirical formula to approximate the SPP attenuation process as a function of radius.

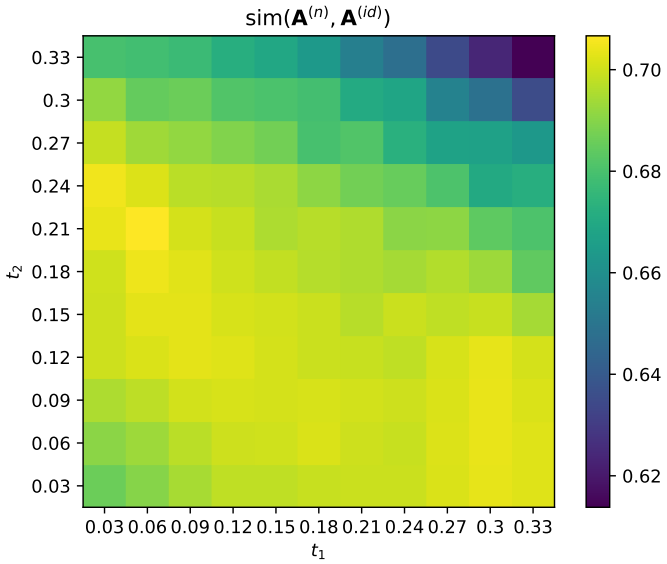

Figure S1: Two-dimensional scan results of the performance of a far-field four-channel emission sample with respect to the two parameters t_1 and t_2. The optimal far-field distribution is achieved at parameters $t_1 = 0.06$ and $t_2 = 0.21$.

2 Performance of Metasurfaces with Deviations in Nano-scatterers

Due to limitations in fabrication precision, the actual shape and size of each nano-scatterer may randomly deviate from the ideal design. This deviation can lead to discrepancies in the scattering polarization states and scattering amplitude from the designed values, thereby affecting the performance of the metasurface. In Figures 3(c) and 3(d) of the main manuscript, we calculate the performance degradation resulting from these two types of deviations and compare the robustness of the proposed metasurface composed of identical nano-scatterers to that of traditional gridded metasurfaces with continuous amplitudes and polarization states. This section will describe the methods and results of these computations in details.

2.1 Deviation in Scattering Polarization States

For any nano-scatterer i, its designed polarization state is $|\lambda_i\rangle$. The actual manufactured nano-scatterer, however, exhibits a polarization state $\left|\lambda_i^{(dev)}\right\rangle$. Without loss of generality, we can plot the designed polarization vector and the deviated polarization vector on the Poincaré sphere, with corresponding vectors to be v_i and $v_i^{(dev)}$, respectively. The angle between these two vectors is α, which indicates the magnitude of the deviation of the polarization state; the plane formed by the line connecting the endpoints of v_i and $v_i^{(dev)}$ and the original vector v_i forms an angle β with the plane formed by v_i and the polar axis. This angle β indicates the direction of the deviation of the polarization state. The angle α follows a Gaussian distribution centered at $\alpha = 0$ with a standard deviation of Δ_p. The angle β follows a uniform distribution between 0 and 2π. The corresponding probability distribution functions are:

$$f(\alpha) = \frac{1}{\sqrt{2\pi\Delta_p^2}} e^{-\frac{\alpha^2}{2\Delta_p^2}}, \tag{S15}$$

$$f(\beta) = \begin{cases} 1/2\pi & ,0 < \beta < 2\pi; \\ 0 & ,\text{otherwise.} \end{cases} \tag{S16}$$

On the Poincaré sphere, we can observe that the sampling method used ensures that $\left|\lambda_i^{(dev)}\right\rangle$ is relatively uniformly distributed around $|\lambda_i\rangle$, as illustrated in Figure S2. This serves as a good model for representing the random deviation of polarization states. We then calculate the correlation coefficient between the far-field distribution with and without deviation. Using Δ_p as the horizontal axis and the correlation coefficient as the vertical axis, we plot the results, which correspond to Figure 3(c) in the main manuscript.

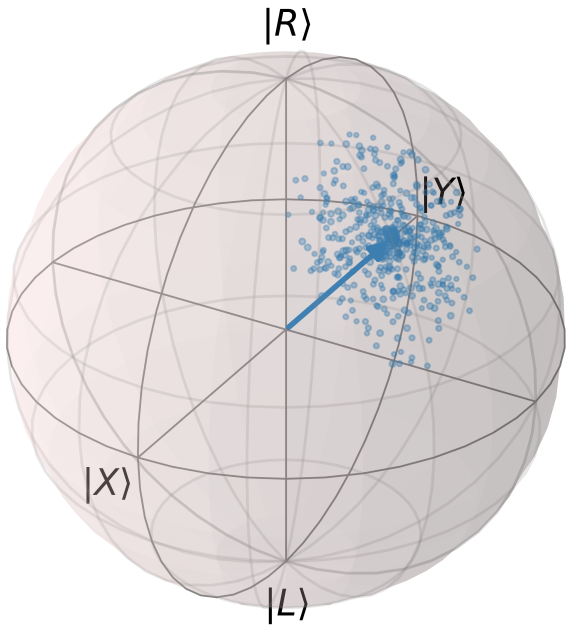

Figure S2: Deviation of the scattering polarization state visualized on the Poincaré sphere. The vector denotes unbiased state $|\lambda_i\rangle$, while the points denote biased state $\left|\lambda_i^{(dev)}\right\rangle$

2.2 Deviation in Scattering Amplitudes

For any nano-scatterer i, its scattering amplitude is denoted as A_i. In the absence of deviations, for the proposed metasurface composed of identical nano-scatterers, $A_i = 1$, $\forall i$; for traditional gridded metasurfaces with continuous amplitudes and polarization states, A_i can be any positive real number. When there are random deviations in the scattering amplitudes, we have:

$$A_i^{(dev)} = A_i\,(1+u)\,, \tag{S17}$$

where the random variable u follows a uniform distribution centered at $u = 0$ with a range of Δ_a. Its probability distribution function is given by:

$$f(u) = \begin{cases} 1/\Delta_a & , -\Delta_a/2 < u < \Delta_a/2; \\ 0 & , \text{otherwise.} \end{cases} \tag{S18}$$

The magnitude of Δ_a indicates the extent of amplitude deviation. For any given Δ_a, we calculate the correlation coefficient between the far-field distribution with and without amplitude deviation. A sample size of 20 is taken to compute the average and standard deviation. Using Δ_a as the horizontal axis and the correlation coefficient as the vertical axis, we plot the results, which correspond to Figure 3(d) in the main manuscript.

2.3 Impact of the Number of Nano-scatterers on Performance Robustness

Increasing the number of nano-scatterers will enhance the metasurface's averaging effects against random deviations of the nano-scatterers, thereby improving robustness in reconstruction performance. To illustrate this point, the three red curves in Figure S3 depict the emission performance curves of traditional gridded metasurface with continuous amplitude and polarization states under three different grid sizes (i.e., with three different numbers of nano-scatterers, as the metasurface area remains constant) in response to random deviations of the nano-scatterers. As expected, smaller grid sizes and a greater number of nano-scatterers result in slower performance decline speed of the metasurface. Specifically, at $d = 300$ nm, corresponding to approximately 1.0×10^4 nano-scatterers, the traditional gridded metasurface with continuous amplitude and polarization states exhibits similar performance robustness to the proposed intelligent-algorithm derived metasurface with identical nano-scatterers (represented by the blue curve in the figure, with approximately 1.5×10^3 nano-scatterers). Therefore, the proposed metasurface exhibits better robustness against deviations in scattering properties of nano-scatterers compared with traditional gridded metasurface with continuous amplitude and polarization states, if the numbers of nano-scatterers are the same.

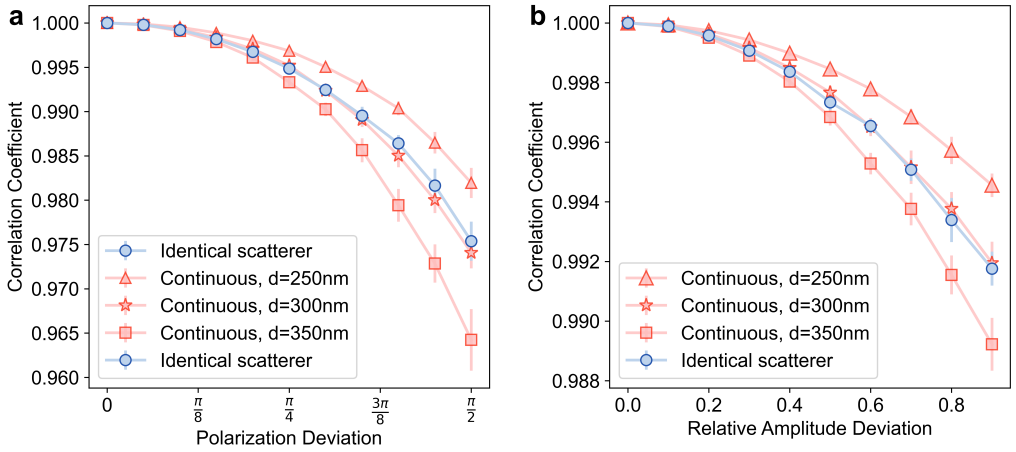

Figure S3: Variation curves of the emission performance of the proposed metasurface composed of identical nano-scatterers (blue line) and traditional gridded metasurface with continuous amplitude and polarization state (red lines) with increasing random deviations of the nano-scatterers. **a**: Deviations in the polarization state of each nano-scatterer; **b**: Deviations in the scattering amplitude of each nano-scatterer. Here, d signifies the grid size of the gridded metasurface, with $d = 250$ nm, 300 nm, and 350 nm corresponding to nano-scatterer's number of 1.5×10^4, 1.0×10^4, and 7.7×10^3, respectively. It can be observed that the gridded metasurface with $d = 300$ nm exhibits comparable performance robustness to the proposed intelligent-algorithm metasurface with identical nano-scatterers in the main manuscript, which consists of only approximately 1.5×10^3 nano-scatterers.

3 Numerical Simulation

3.1 Detailed Description of the Numerical Simulation

After obtaining the designed metasurface structure using the Intelligent Algorithm, we utilize the COMSOL Multiphysics for numerical simulations. The metasurface is modeled as a silver plate with etched nanogrooves as nano-scatterers. The origin is set at the center of the silver layer top surface. A z-polarized electric dipole point source is placed 20 nm above the origin and the wavelength is set to be 632.8 nm. At this wavelength, silver has a refractive index of $n_{sil} = \sqrt{\epsilon_{sil}} = 0.056253 + 4.2760i$, resulting in a SPP effective refractive index of $n_{spp} = \sqrt{\frac{\epsilon_{sil}\epsilon_{air}}{\epsilon_{sil}+\epsilon_{air}}} = 1.0285 + 0.00078253i$ for the SPP wave propagating on the silver-air interface. Consequently, the SPP wavelength on the sample surface is 615.3 nm with a propagation length of 64.3 μm.

Positions of the nanogrooves obtained through the intelligent algorithm $(\bar{x}_i^f, \bar{y}_i^f)$ are imported into COMSOL Multiphysics for modeling and simulation, allowing us to simulate the electric field distribution on the metal surface. Then, we use the Kirchhoff diffraction integral formula to compute the total scattered field distribution in the far field by selecting the integration area to be the openings of all nanogrooves at z=0 plane.

3.2 Simulation Results of Metasurfaces for Other Emission Patterns

To demonstrate the capability of the proposed metasurface in the vectorial manipulation of emission field (amplitude and polarization), we present numerical simulation results for other metasurface structures designed by the proposed intelligent algorithm. These include far-field simulation results for emitting four beams of light with identical LCP polarization in four different directions and for emitting two LCP beams and two RCP beams in four different directions (Figure S4). Results for emitting five beams with different polarization states (two LCP, two RCP, and one linearly polarized) are presented in Figure S5 as a typical design case without centro-symmetry. Results for emitting eight beams with 8 different polarization states (including different linear, ciucular and elliptical polarizations, as the most general case) are provided in Figure S6. Additionally, to further demonstrate the capability to achieve complex emission patterns and polarization control in the far field, simulation results of a ring-shaped light field with radial polarization distribution (characterized by a ring-shaped intensity distribution and radially polarized at each point on the ring) are provided (Figure S7). From the field distribution diagrams of different polarization components obtained through simulations, it is evident that the designed metasurface's far-field emission intensity and polarization distribution align with the design targets. This further validates that the proposed intelligent algorithm possesses excellent independent control over the polarization and amplitude distribution of the far-field emission of the metasurface.

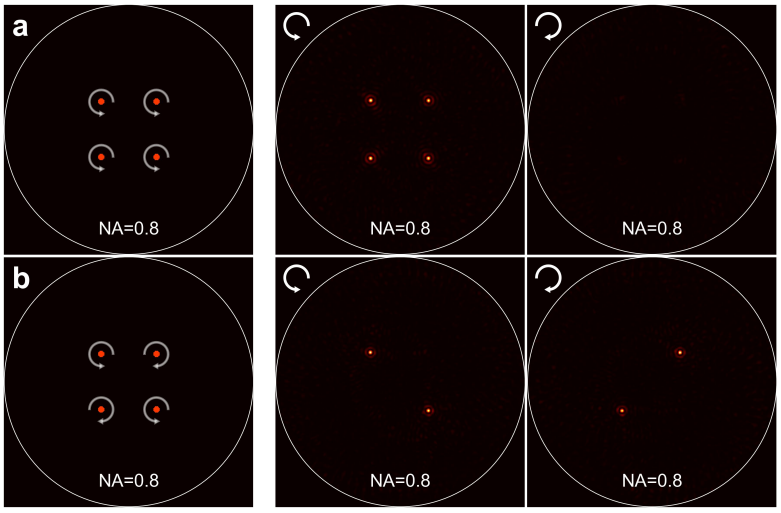

Figure S4: Metasurface emitting four collimated beams with independently controllable polarization states. **a**: Simulation results for four beams, all polarized as LCP light. **b**: Simulation results for four beams, with two polarized as LCP and two as RCP light. The figures display, from left to right, the target intensity distribution and polarization states in the far field, as well as the simulated intensity distributions of the LCP and RCP polarization components.

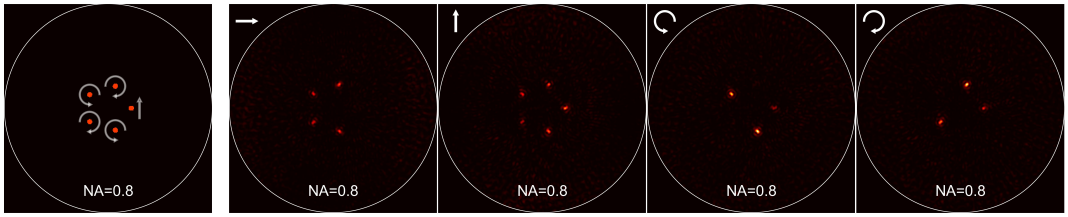

Figure S5: Metasurface emitting five collimated beams with independently controllable polarization states (two LCP beams, two RCP beams, and one linearly polarized beam in vertical direction(Y)), presented as a typical design case without centro-symmetry. The figures display, from left to right, the target intensity distribution and polarization states in the far field, as well as the simulated intensity distributions of the X, Y, LCP, and RCP polarization components.

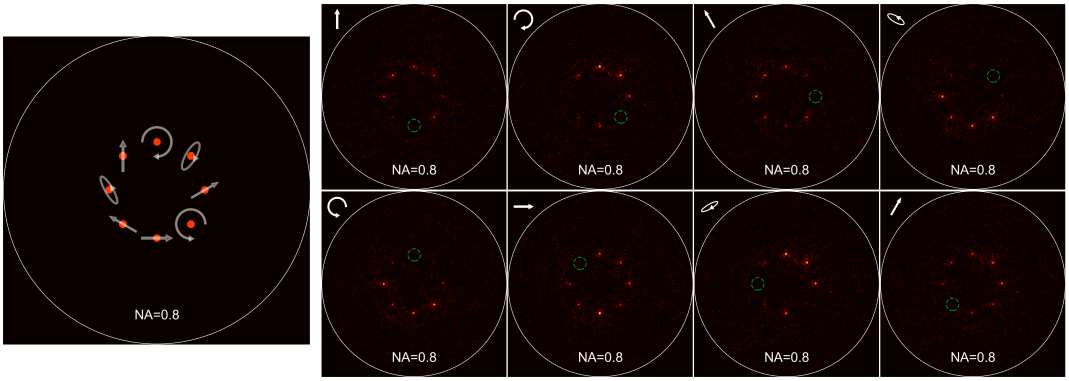

Figure S6: Metasurface emitting eight collimated beams with independently controllable polarization states (including different linear, ciucular and elliptical polarizations). The left figure displays the target intensity distribution and polarization states in the far field. Other figures display the simulated intensity distributions of the polarization components orthogonal to the target polarizations. The eight emitted beams exhibit extinction one by one (marked with green circles), indicating that their polarization states meet the design requirements.

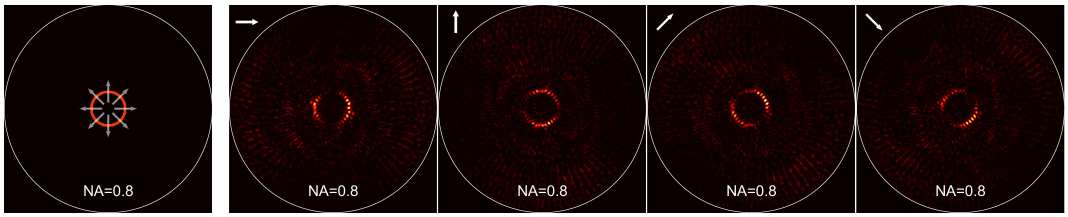

Figure S7: Metasurface emitting ring-shaped light with radial polarization. The figures display, from left to right, the target intensity distribution and polarization states in the far field, as well as the simulated intensity distributions of the X, Y, $+45°$, and $-45°$ linear polarization components.

4 Experiment

4.1 Sample Fabrication

Firstly, a silver film with a thickness of 260 nm was deposited on a glass substrate by electron beam evaporation. Then, the designed metasurface structure was fabricated by direct focused ion beam milling. The scanning electron microscope (SEM) image of a metasurface sample is shown in Figure S8. Except for the outer nano-scatterers, there is an circular laser coupler in the center of the image. It is observed that the fabricated nanogrooves are not quite uniform. The reason is that the silver film evaporated by electron beam evaporation is a polycrystal film which is made up of grain structures with different sizes (Figure S8). This inhomogeneity will lead to decreased linear polarization purity and intensity uniformity of the scattered light of the nanogrooves in experiments. In principle, homogeneous nanogrooves and better experimental results can be obtained by using chemically synthesized single-crystal silver film[2] or using other advanced fabrication techniques (such as the template stripping method[3]).

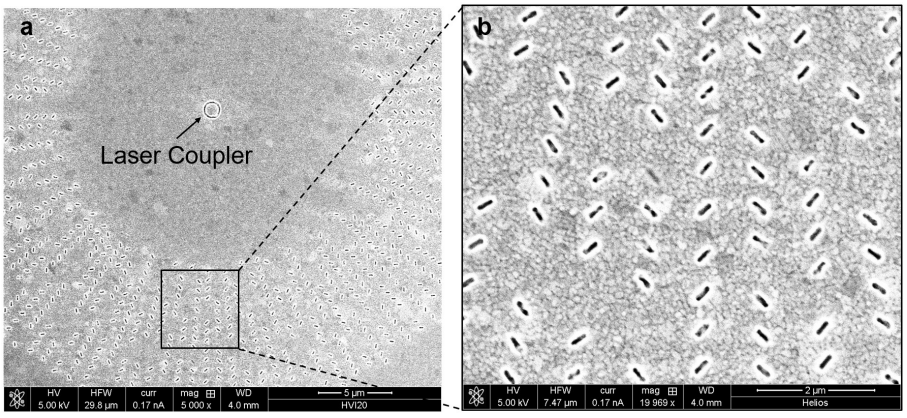

Figure S8: **a** SEM image of a typical metasurface sample. **b** Enlarged plot of the box in **a** for detailed view of the nano-scatterers.

4.2 Experimental Setup

In the experiment, a He-Ne laser with $\lambda = 632.8$ nm is used, as schematically shown in Figure S9. The incident laser passes through an adjustable attenuator and a polarizer before entering a vortex waveplate, which converts the linearly polarized light to radially polarized light. This radially polarized light is then focused by an objective (100×, NA=0.8) onto the laser coupler at the center of the metasurface. The laser coupler converts the radially polarized incident light into isotropic and radially outward-propagating SPPs on the metal surface. These SPPs are scattered by the outer nano-scatterers, with the scattered light collected by the same objective and directed to the far field. An LED for illuminating with white light is also included in the microscope assembly to illuminate and positioning the sample. A spatial filter is placed on the image plane of the sample to filter out the directly scattered light from the laser coupler and the reflected incident laser. A 4F imaging system follows, equipped with a switchable $\lambda/4$ waveplate and a polarizer to extract different polarization components. Finally, a CCD camera measures the intensity distribution of each polarization component. There is a switchable lens in front of the CCD. The

distance between the lens and the CCD equals the focal length, allowing measurement of the intensity distribution of the Fourier plane (i.e., the far-field intensity distribution) with the lens in the path; otherwise, it measures the sample's image plane (i.e., the light intensity distribution on the metasurface structure's surface).

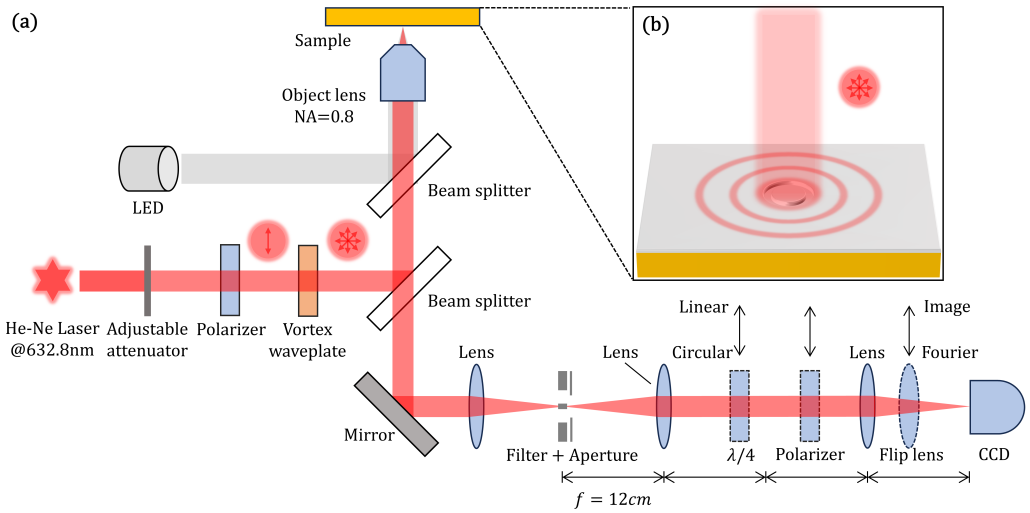

Figure S9: **a** Schematic of the experimental setup. Red arrows indicate the polarization state of the laser at these points, and vertical black arrows indicate optical elements that can be switched into or out of the optical path for different measurement purposes. **b** Schematic of the laser coupler converting radially polarized incident light into radially outward-propagating SPPs.

4.3 Experimental Results

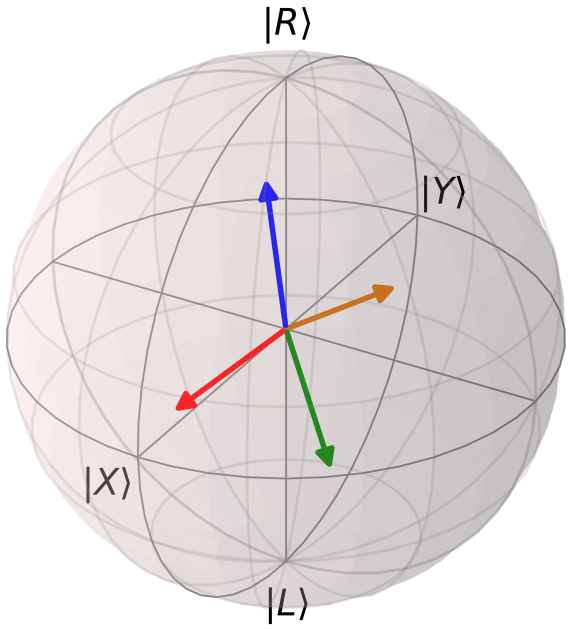

Figure S10: Reconstructed polarization states of the four beams emitted from the metasurface sample visualized on the Poincaré sphere. The design targets are color-coded: Red for X linear polarization, Orange for Y linear polarization, Blue for LCP (L) , and Green for RCP (R).

Using the described experimental setup, the intensity distributions of various polarization components can be detected by switching the $\lambda/4$ waveplate and changing the polarizer's orientation. Further processing of CCD images of these intensity distributions allows extraction of the polarization state information of different far-field emission spots. Here, we employ the Maximum Likelihood Estimation method[4] to reconstruct the density matrix of the polarization states of the far-field emission spots by acquiring intensity distribution data from linearly polarized channels (X, Y, $+45°$, $-45°$) and circularly polarized channels (LCP, RCP). The data for the LCP and RCP channels were corrected for the effect of the $\lambda/4$ waveplate transmittance of $t_{\lambda/4} = 0.8920$. Considering that beamsplitters in the optical path can slightly change the light beam's polarization state, the transmission matrix of the optical system was measured to calibrate these effects on the polarization state measurements. Figure S10 presents the experimental results for the metasurface sample emitting four beams with different polarization states, reconstructed using the aforementioned method. The measured polarization purities are 0.73, 0.57, 0.60, and 0.42 for X, Y, LCP, and RCP, respectively. The experimentally reconstructed polarization states somehow deviate from the ideal design targets, primarily due to: (1) imperfections in the fabricated nanogrooves causing deviations in the polarization state and intensity of scattered light from the design values; (2) the influence of scattered background light on measurement results; and (3) limitations in the CCD's dynamic range and spatial resolution, with some pixels saturating and resolution being low.

References

[1] Matthew Pasienski and Brian DeMarco. A high-accuracy algorithm for designing arbitrary holographic atom traps. *Optics express*, 16(3):2176–2190, 2008.

[2] Jer-Shing Huang, Victor Callegari, Peter Geisler, Christoph Brüning, Johannes Kern, Jord C Prangsma, Xiaofei Wu, Thorsten Feichtner, Johannes Ziegler, Pia Weinmann, et al. Atomically flat single-crystalline gold nanostructures for plasmonic nanocircuitry. *Nature communications*, 1(1):150, 2010.

[3] Tatsuro Endo, Hirotaka Yamada, and Kenji Yamada. Template stripping method-based au nanoarray for surface-enhanced raman scattering detection of antiepileptic drug. *Micromachines*, 11(10):936, 2020.

[4] Jiangwei Shang, Zhengyun Zhang, and Hui Khoon Ng. Superfast maximum-likelihood reconstruction for quantum tomography. *Phys. Rev. A*, 95:062336, Jun 2017.